# Chapter 1

# Introduction

## 1.1 What are Gravitational Waves ?

Gravitational waves are radiative solutions of any theory of gravity respecting special relativity. In Einstein's general relativity (GR), the gravitational field is described by the curvature of space-time, the source of this curvature being the stress-energy tensor. A time-varying stress-energy tensor results in time-varying space-time curvature of distant space-time points. Therefore, in GR, gravitational waves (GW) are ripples in the curvature of space-time propagating through space-time itself.

In GR, GW travel at the speed of light and like electromagnetic (EM) waves are transverse and have two independent states of polarisation. However, GW have crucial differences from EM waves. Since photons do not carry charge, Maxwell field equations are linear. However, gravitons carry energy and momentum [2] and therefore are themselves sources of gravity. The mathematical reflection of this fact is that Einstein's field equations comprise a set of non-linear partial differential equations. This nonlinearity prevents us from finding general wave-like solutions of the exact Einstein equations. However, for weak GW, whose propagation is primarily determined by the energy and momentum of the material source, wave-like solutions can easily be found. We briefly indicate how the null propagation, transverse nature, and the two polarisation states of GW arise in GR in the linearised gravity limit.

Before we proceed it is worthwhile mentioning that the existence of GW has already been *indirectly* confirmed. This comes from the discovery of the famous Hulse-Taylor binary pulsar PSR B1913+16 [3] and the measured decay of its orbital period (see [4] for an update and references therein) . The binary system emits GW which carry energy away from it and causes the two objects to revolve around each other in orbits of steadily decreasing size. The measured rate of change of the orbital period is found to be equal to $1.01 \pm 0.001$ times the GR prediction for gravitational radiation damping [5]. This is the first confirmation of Einstein's GR beyond the standard Solar system tests in a strong-field scenario where nonlinearities and radiation effects are not negligible. The excellent agreement of observation with theory conclusively shows the existence of GW, at the level predicted by GR. We shall return again to the Hulse-Taylor binary pulsar test later in this Chapter.

### 1.1.1 GW in linearised gravity

A weak GW produces a small space-time curvature in its region of propagation. The metric $g_{\mu\nu}$ in the far-zone in Cartesian-like coordinates $x^\mu$ is therefore quasi-Minkowskian.

$$g_{\mu\nu} = \eta_{\mu\nu} + h_{\mu\nu} \tag{1.1}$$

where $\eta_{\mu\nu}$ is the Minkowski metric and $h_{\mu\nu}$ is the metric perturbation due to the weak GW ($|h_{\mu\nu}| << 1$). Linearising the vacuum Einstein equations by discarding all terms second order in $h_{\mu\nu}$ in the Ricci tensor, we get a set of 10 *linear* partial differential equations for the 10 independent $h_{\mu\nu}$.

$$\Box h_{\mu\nu} - \partial_\mu V_\nu - \partial_\nu V_\mu = 0 \tag{1.2}$$

where $V_\mu = \partial_\alpha h^\alpha_\mu - \frac{1}{2}\partial_\mu h^\alpha_\alpha$ and $\Box$ is the flat-space d'Alembertian operator. The 10 equations in Eq. (1.2) are not functionally independent because of the four Bianchi identities and thus four degrees of freedom among the 10 $h_{\mu\nu}$ correspond to general coordinate transformations involving four arbitrary functions $x'^\mu(x)$. However, we will consider only those classes of transformations which preserve the form of the metric given in Eq. (1.1). These are

$$x'^\mu = x^\mu + \xi^\mu(x) \tag{1.3}$$

where $\xi^\mu(x)$ are arbitrary functions apart from being of the same order of smallness as the metric perturbations. By fixing the 4 functions $\xi^\mu(x)$ we finally determine the metric. The choice of gauge (called the Lorentz gauge) is such that in the coordinates $x'^\mu$ the vector $V_\mu$ vanishes. The Einstein equations which reduces simply to the flat-space wave-equations for each of the metric components lead to the following superposition of plane waves

$$h_{\mu\nu} = \int d^3k\, a_{\mu\nu}(\mathbf{k}) e^{i(\omega t - \mathbf{k}.\mathbf{x})} \tag{1.4}$$

with $\omega = |\mathbf{k}|$, where $x^\mu = (t, \mathbf{x})$, $k^\mu = (\omega, \mathbf{k})$ being the wave-vector. The relation $\omega = |\mathbf{k}|$ explicitly shows that GW propagate with the speed of light. The wave amplitudes $a_{\mu\nu}(\mathbf{k})$ are constants which have to satisfy the Lorentz gauge condition. Now, the Lorentz gauge condition is left unaltered by further gauge transformations by functions $\xi^\mu(x)$ which satisfy the flat-space wave equation. These conditions are used to make any four of the metric components vanish. If we make $h_{ti} = h^\mu_\mu = 0$, the Lorentz gauge condition imposes the relations $h_{tt} = 0$ and $k^j a_{ij}(\mathbf{k}) = 0$. The last condition shows that the amplitude is orthogonal to the wave-vector, and therefore, gives us the transverse nature of GW. We are left with two non-zero components of the wave-amplitudes which correspond to the two states of polarisation. Let us re-orient the spatial axes such that the z-axis coincides with $\mathbf{k}$. Then, the GW mode corresponding to a frequency $\omega(= |\mathbf{k}|)$ and propagating along the z-axis is given by

$$h_{\mu\nu}(t, z) = \begin{bmatrix} 0 & 0 & 0 & 0 \\ 0 & a_{xx} & a_{xy} & 0 \\ 0 & a_{xy} & -a_{xx} & 0 \\ 0 & 0 & 0 & 0 \end{bmatrix} e^{i\omega(t-z)} \tag{1.5}$$

Because of the explicit representation of the transverse and traceless conditions above, the coordinates in which Eq. (1.5) are written are called *transverse-traceless* (TT) gauge.

### 1.1.2 Generation of GW: application to compact binaries

We now turn to the problem of relating the GW amplitude and frequency (or, alternatively, the two polarisations) to the properties of the source which generates the wave. For this purpose, our starting point is Einstein's equations with a source term described by the energy-momentum tensor $T_{\mu\nu}$. We assume that the source is moving slowly enough to allow the linear approximation of the GW amplitude. In terms of the trace-reversed amplitude $\bar{h}_{\mu\nu} = h_{\mu\nu} - \frac{1}{2}\eta_{\mu\nu}\, h$, Einstein's equations reduce, in the Lorentz gauge, to

$$\Box \bar{h}_{\mu\nu} = 16\pi\, T_{\mu\nu}. \tag{1.6}$$

The metric perturbation which satisfies the above equation is given, at a field point $(t, \mathbf{x})$, by the following retarded integral over the source $T_{\mu\nu}$ (no incoming waves)

$$\bar{h}_{\mu\nu}(t, \mathbf{x}) = 4 \int \frac{T_{\mu\nu}(t - |\mathbf{x} - \mathbf{x}'|, \mathbf{x}')}{|\mathbf{x} - \mathbf{x}'|}\, d^3x'. \tag{1.7}$$

$\bar{h}_{\mu\nu}(x)$ still has to satisfy the Lorentz gauge condition, which for the trace-reversed metric, is simply $\partial_\nu \bar{h}_{\mu\nu} = 0$. This condition simply reduces to the linearised conservation law of energy-momentum and is therefore identically satisfied. Let us assume a source varying sinusoidally with time, *i.e.*, $T_{\mu\nu}(t, \mathbf{x}) = \tilde{T}_{\mu\nu}(\mathbf{x}) \cos \omega t$. Let us also assume that the wavelength $\lambda = 2\pi/\omega$ of the emitted radiation is much larger than the characteristic dimension $R$ of the source ($\lambda >> R$). The retarded integral Eq. (1.7) at a field point spatially far apart from the source reduces to

$$\bar{h}_{\mu\nu}(t, \mathbf{x}) = \frac{4}{R} \int \tilde{T}_{\mu\nu}(\mathbf{x}') \cos \omega(t - R)\, d^3x', \tag{1.8}$$

where $R$ is the distance to the source with $R \to \infty$. The condition $R \to \infty$ allowed us to neglect the variation of $\mathbf{x}'$ over the source in the denominator of the retarded integral in Eq. (1.7), while the condition $\lambda >> R$ allowed us to replace $\cos \omega(t - |\mathbf{x} - \mathbf{x}'|)$ by $\cos \omega(t - R)$. Even though from the R.H.S. of Eq. (1.8) the GW amplitude at infinity appears to be spherically symmetric, it depends on the direction of the field-point with respect to the source. This is because $\bar{h}_{\mu\nu}(t, \mathbf{x})$ satisfies the TT gauge condition, the choice of which depends on the direction of propagation of the GW.

Now, by the TT gauge condition, $\bar{h}_{t\nu}(t, \mathbf{x}) = 0$. Hence, we only require the spatial components $\int T_{ij}(t - R, \mathbf{x}')\, d^3x'$ of the source, where we have re-absorbed the time-dependence into the energy-momentum tensor components. Evaluating these retarded integrals for a bounded source and using the local energy-momentum conservation, the relevant spatial components of the metric perturbation become

$$\bar{h}^{ij}(t, \mathbf{x}) = \frac{2}{R} \frac{d^2}{dt^2} \int (x')^i (x)'^j T^{tt}(t - R, \mathbf{x}')\, d^3x'. \tag{1.9}$$

For a weak source the energy density $T^{tt}(t, \mathbf{x}')$ is dominated by the rest-mass density $\rho(t, \mathbf{x})$.

Introducing the *mass quadrupole moment* of the source as $I^{ij}(t) = \int x^i x^j \rho(t, \mathbf{x})\, d^3x$, we have

$$\bar{h}^{ij}(t, \mathbf{x}) = \frac{2}{R}\frac{d^2}{dt^2} I^{ij}(t - R) \tag{1.10}$$

Even though the above derivation neglects self-gravitating systems, Eq. (1.10) applies for slowly moving self-gravitating systems like binary stars whose orbits are described by Newtonian mechanics [6, 7]. Let us now make an order-of-magnitude estimate of the GW amplitude from typical binary systems like the Hulse-Taylor binary pulsar. Let us assume that the binary consists of two compact objects of individual masses $m_1$ &$m_2$, total mass $m$ ($m = m_1 + m_2$), reduced mass $\mu$ and their relative separation is r. Modelling the stars as point particles, we assume them to describe circular orbits about their common centre-of-mass. Since the centre-of-mass motion is conserved, we concentrate only on the relative motion which is also circular with radius $R$. The quadrupole moment becomes $I^{ij} \sim \mu R^2$ and two time-derivatives in RHS of Eq. (1.10) are replaced by two factors of the orbital period $P$. By Kepler's law, $r = (m P^2)^{1/3}$. The GW amplitude is, then, of the order

$$h^{ij} \sim \frac{1}{R}\frac{\mu r^2}{P^2} = \frac{1}{R}\frac{\mu}{P^2}(m P^2)^{2/3} = \frac{1}{R}\frac{\mathcal{M}^{5/3}}{P^{2/3}}, \tag{1.11}$$

where $\mathcal{M}^{5/3} = m^{5/3}\nu$ is the *chirp-mass* and $\nu = \frac{m_1 m_2}{m^2}$ is the *symmetric mass-ratio*, $m_1, m_2$ being the individual masses. The quantities $\mathcal{M}$, $\nu$ are very useful quantities in the physics of inspiralling compact binaries, as we will see in the following sections and subsequent chapters of this thesis. Putting back the factors of G & c, we get the following estimate

$$h^{ij} \sim 10^{-21}\left(\frac{100\,\mathrm{pc}}{R}\right)\left(\frac{\mathcal{M}}{M_\odot}\right)^{5/3}\left(\frac{1\,\mathrm{hour}}{P}\right)^{2/3} \tag{1.12}$$

We provide now a more concrete analysis of the GW from a binary. Let us first orient the z-axis orthogonal to the binary orbit and study the GW emitted by the binary in this direction at infinity. In the asymptotic limit, in a small solid angle about the direction of propagation, the GW can be approximated as a plane wave. The relative position, for a circular orbit of radius $R$ and angular velocity $\omega$ is $\mathbf{x}' \equiv (x', y', z') = (r\cos\omega t, r\sin\omega t, 0)$. The non-zero components of the quadrupole moments are $I_{xx} = \frac{1}{2}\mu r^2(1 + \cos 2\omega t)$, $I_{xy} = I_{yx} = \frac{1}{2}\mu r^2 \sin 2\omega t$, $I_{yy} = \frac{1}{2}\mu r^2(1 - \cos 2\omega t)$. Inserting them in Eq. (1.10), the GW at infinity in a direction perpendicular to the orbital plane is

$$h^{\mu\nu} = -\frac{4}{z}\mathcal{M}^{5/3}\omega^{2/3}\begin{bmatrix} 0 & 0 & 0 & 0 \\ 0 & \cos[2\omega(t-z)] & \sin[2\omega(t-z)] & 0 \\ 0 & \sin[2\omega(t-z)] & -\cos[2\omega(t-z)] & 0 \\ 0 & 0 & 0 & 0 \end{bmatrix} \tag{1.13}$$

The metric perturbation in Eq. (1.13) satisfies the TT gauge for a plane wave propagating along the z-direction. Hence, we can compare Eq. (1.13) with Eq. (1.5) and immediately come to the important conclusion that, at the leading order, the GW frequency is *twice* the orbital frequency of the binary.

### 1.1.3 The GW energy flux at infinity: Einstein's Quadrupole Formula

In this subsection we indicate how one arrives at the energy carried by linearised GW to the far-zone. From the EM wave analogy, we know that the energy flux, given by the Poynting vector, is quadratic in the fields which in turn are derivatives of the potentials. However, in GR , one cannot construct the GW energy flux as an expression which is quadratic in the first derivatives of the metric. Such a quantity would be local and will vanish in the locally-inertial frame because of the Equivalence Principle. Still, one can have an *approximate* notion of energy flux of a weak GW whose wavelength $\lambda$ is much smaller than the scale of space-time curvature $\mathcal{R}$. This approximation becomes more accurate if we perform our calculation in a space-time region far way from the material source. Now, to define the energy flux of GW, we need an energy-momentum tensor of the GW itself. To obtain this, we have to start again from Einstein's equations in vacuum with the ansatz Eq. (1.1) but keep terms upto second order in $h_{\mu\nu}$. The resulting expression will be like Eq. (1.2), but with the RHS containing terms second order in $h_{\mu\nu}$ instead of 0.

$$\Box h_{\mu\nu} = \Big(\text{Terms 2nd order in } h_{\mu\nu}\Big), \tag{1.14}$$

where we have used the Lorentz gauge. Comparing Eq. (1.14) with the wave equation of linear GW with a *material* source (Eq. (1.6)), we see that the quantity in the RHS of Eq. (1.14) (divided by $16\,\pi$) can be defined as the effective energy-momentum tensor $T^{(GW)}_{\mu\nu}$ of the linear GW. We, of course, do not need to re-solve Einstein's equations with this term as that would take us beyond the linear approximation. The quantity $T^{(GW)}_{\mu\nu}$ will act as a source for the GW (in addition to the material $T_{\mu\nu}$) only in the next order calculation. The energy flux, for a plane GW propagating along the z-axis in the asymptotic quasi-Minkowskian region, is simply $T^{(GW)}_{tz}$. However, in the short-wavelength approximation the energy flux, has to be defined as an average of $T^{(GW)}_{tz}$ over space-time volumes whose dimensions are large compared to $\lambda$ but small compared to $\mathcal{R}$. The total power radiated can be obtained by integrating over all possible directions the quantity $T^{(GW)}_{ti}\,n^i$ where $n^i$ is an unit-vector along any direction. The final result of the long, but straightforward average over the angular directions, is the following expression for the GW flux at infinity $L$

$$L = (1/5)\langle \frac{d}{dt}\left(\ddot{I}_{ij}\right)\frac{d}{dt}\left(\ddot{I}_{ij}\right)\rangle, \tag{1.15}$$

where the angular-brackets indicate averaging over the time-scale of the variation of the source. This is the famous Einstein's quadrupole formula.

### 1.1.4 Effect of GW on test-particles: plus & cross polarisations

Consider a plane GW travelling along the z-axis, but with $h_{xy} = 0$ and two test particles lying on the x-axis at rest and separated by a length $L_0$ before the passing of the GW. To linear order in $h_{\mu\nu}$ , the GW leaves the coordinate positions of each of them unchanged. But the proper distance between the two particles is not $L_0$, the altered distance being (again, to linear order in $h_{\mu\nu}$)

$$L(t) = L_0\left(1 + \frac{1}{2}h_{xx}(t,0)\right) \tag{1.16}$$

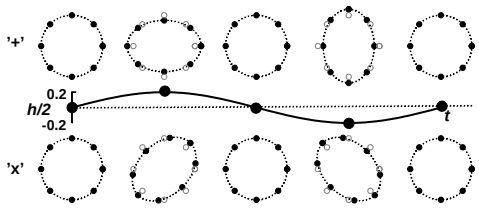


Figure 1.1: Effect of plus and cross polarised GW on a ring of test-particles lying perpendicular to the direction of propagation. Expansion and contraction in mutually perpendicular directions is a manifestation of the traceless nature of GW. The angle between the two independent polarisation states is $\frac{\pi}{4}$. Adapted from Ref. [8].

If the particles are placed along the y-axis the distance between them varies with time as $L_0\left[1-\frac{1}{2}h_{xx}(t,0)\right]$. Thus an expansion of space in the x-axis is accompanied by a contraction along the y-axis. This fact, of course, is a manifestation of the traceless condition. The action on a ring of test particles arranged on the xy-plane is shown in the first row of figures in Fig. 1.1. Because of this pattern a GW of the form in Eq. (1.5) with $h_{xy}=0$ is called a "plus-polarised" GW and is denoted by $h_+$. On the other hand, a GW with $h_{xx}=0$ will produce a pattern shown in the second row of figures in Fig. 1.1. Because of the shape of the pattern, such a wave is called a "cross-polarised" GW and is denoted by $h_\times$. Note that the one pattern can be obtained by rotating the other by an angle of 45 degrees. In general, a GW will be a superposition of the two polarisations and can be written as

$$h_{\mu\nu}(t,z)=\begin{bmatrix} 0 & 0 & 0 & 0\\ 0 & h_+(t-z) & h_\times(t-z) & 0\\ 0 & h_\times(t-z) & -h_+(t-z) & 0\\ 0 & 0 & 0 & 0 \end{bmatrix}, \tag{1.17}$$

the ratios of magnitudes and the phase-differences of $h_+$ & $h_\times$ determining the various states of polarisation.

We now compare Eq. (1.17) with Eq. (1.13) which also represents a plane wave propagating in the z-direction. In the case of the GW in Eq. (1.13), the phase difference between the two polarisation amplitudes is $\frac{\pi}{2}$. Therefore, in a direction perpendicular to the orbital plane of a binary system, the GW will have *circular* polarisation. It is also clear that the state of polarisation will depend on the direction of propagation.

## 1.2 Detection of GW with Laser Interferometers

The changes in relative positions of test-particles in a GW allows for a *direct* determination of these waves. For this purpose, we return to the arrangement of Eq. (1.16) where two test-particles lie on the x-axis and a plus polarised GW is travelling along the z-axis. Let us define a quantity called the GW *strain* given by the fractional change in length between two

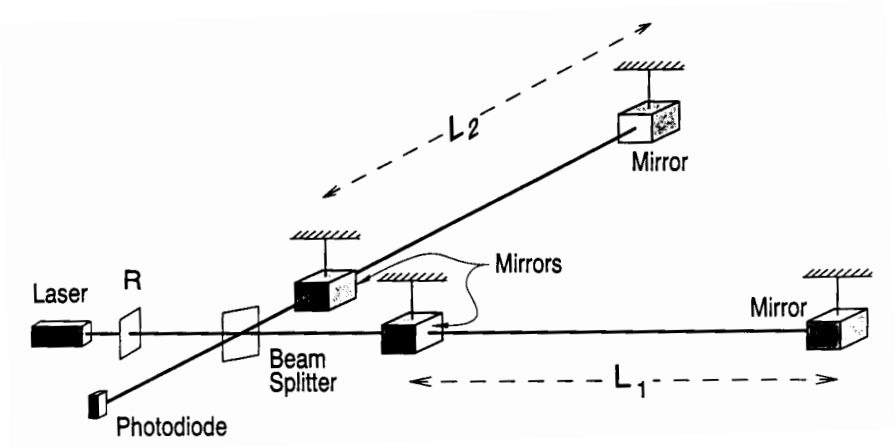


Figure 1.2: Schematic diagram of a Laser interferometric GW detector. Adapted from Ref. [9].

test-masses. The GW strain, $\frac{\delta L}{L_0}$ is given by

$$\frac{\delta L}{L_0}(t) = \frac{1}{2}h_+(t,0) \tag{1.18}$$

This strain can be measured in a Michelson-type interferometer as follows. Four masses are freely suspended from vibration-isolated supports in an 'L' shaped configuration as shown in Fig 1.2. Each pair of masses comprise each arm of the detector (of nearly equal lengths). An incident GW would cause the lengths of the two-arms to change unequally with time. The arm-length difference can be measured by interferometric methods by placing a beam-splitter at the junction of the two arms and attaching mirrors to the suspended masses at the two arm-ends. By monitoring the interference pattern over time both the amplitude and frequency of the GW can be measured.

The extreme weakness of the gravitational interaction prevents a simple implementation of the above described detection mechanism in laboratory length scales. Based on typical astrophysical sources, compact binaries being the most plausible of them, the typical strain $h$ one has to measure in order to detect a GW was shown to be $\sim 10^{-21}$ in Section (1.2). For a given sensitivity in measuring $\delta L$, say a billionth of the wavelength of visible light, the strain sensitivity $\frac{\delta L}{L_0}$ can reach $10^{-21}$ for arm-lengths several hundred kilometers long. This difficulty can be overcome by attaching partially reflecting mirrors on the two masses near the beam-splitter (see Fig 1.2). Each arm now acts as a cavity and there are many reflections between the two ends of each arm before the beams are recombined. Due to such effective long arm-lengths, laser beams are used for the interferometric detection of the arm-length differences.

Let us now return to the assumptions made in writing the GW strain in Eq. (1.18). These are a particular state of polarisation of the GW (plus in this case) and the arrangement of the test-masses in a plane perpendicular to the direction of propagation. However, as we mentioned, the state-of polarisation depends on the direction of propagation of the GW with respect to the binary orbit. This direction is characterised by two angles, $\iota$, $\& \psi$. $\iota$ is the angle between the angular momentum vector $\mathbf{L}$ of the binary and the direction of propagation and

is called the *inclination angle*. $\psi$ determines the direction of the projection of $\mathbf{L}$ in a plane normal to the direction of propagation (the plane of the sky) and is called the *polarisation angle*. The detector also need not be aligned perpendicular to the direction of propagation. This factor is taken into account by the two spherical polar coordinates of the source $\theta$, & $\phi$ w.r.t. the detector. The general expression of the GW strain, which we denote from now on by $h$, in the case of arbitrary source location and orientation is

$$h(t) = F_+(\theta, \phi, \psi)\, h_+(t) + F_\times(\theta, \phi, \psi)\, h_\times(t) \tag{1.19}$$

where

$$h_+(t) = -\frac{2\mathcal{M}^{5/3}\omega^{2/3}}{R}(1 + \cos\iota^2)\cos 2\omega t\,, \tag{1.20}$$

$$h_\times(t) = -\frac{2\mathcal{M}^{5/3}\omega^{2/3}}{R}2\cos\iota\,\sin 2\omega t\,, \tag{1.21}$$

$$F_+(\theta, \phi, \psi) = \frac{1}{2}\left(1 + \cos^2\theta\right)\cos 2\phi\,\cos 2\psi - \cos\theta\,\sin 2\phi\,\sin 2\psi\,, \tag{1.22}$$

$$F_\times(\theta, \phi, \psi) = \frac{1}{2}\left(1 + \cos^2\theta\right)\cos 2\phi\,\sin 2\psi + \cos\theta\,\sin 2\phi\,\cos 2\psi\,. \tag{1.23}$$

The functions $F_{+,\times}(\theta, \phi, \psi)$ are called the *beam pattern functions* of the detector (see Ref. [10]).

Interferometric detection of GW is not the only possible method for direct detection of GW. Historically, bar type detectors were the first to search for GW. These are resonant cylinders whose vibrational modes are excited when a GW is incident on them. J. Weber was the first to build a bar detector [11] and announced the detection of GW. However this observation was not reproducible. Since then, several bar detectors have been built like Nautilus, Explorer and Auriga (in Italy), Allegro (in US) and NIOBE (in Australia). However, only the first three are presently operational. We do not discuss the details of bar detectors as the focus of this thesis is interferometric detection.

## 1.3 GW astronomy

A worldwide network of interferometric detectors has been built based on the principles outlined in the previous section. These are *broad band* kilometer scale detectors (*i.e*, physical arm-lengths $\sim$ kms) sensitive to high frequency ($\sim$10-1000Hz) GWs. All are Michelson interferometers and most of them employ Fabry-Perot cavities in the arms to enhance their sensitivities. Different noises in different frequency ranges limit the sensitivity of these types of detectors. In USA, the Laser Interferometer Gravitational wave Observatory (LIGO) [12] has just completed its fifth science run, lasting for 2 years. Near Pisa, the French-Italian Virgo [13] detector is progressing fast towards its science run. The other two detectors, British-German GEO [14] and the Japanese detector TAMA [15] are also operational. LIGO is the largest of these detectors. It comprises two 4-km long L shaped interferometers located at Hanford and Louisiana. A third similar detector with 2-km long arm lengths is also located at Hanford. The LIGO detectors reached their design sensitivity in 2005. The strain sensitivity is maximum at around 100 Hz and is $\sim 10^{-22}$. It is now capable of detecting the

inspiral and merger of a neutron star binary located upto a distance of the Virgo cluster. See Ref. [16] for a recent review of the current status of the various detectors. The construction of the above mentioned detectors, researches in data-analysis strategies, advances in technologies is eventually expected to lead to the development of a new field called *Gravitational Wave Astronomy*. A space-based interferometer called the Laser Interferometer Space Antenna (LISA) is also planned. This interferometer, when launched, will be sensitive to the low frequency ($10^{-4}$ – 1 Hz) GW. We give a more detailed discussion of LISA later in this chapter.

### 1.3.1 Sources for GW astronomy

In this subsection, we give an overview of the types of possible astrophysical sources for GW astronomy. GW sources can be very broadly classified into 4 classes: coalescence events, continuous (periodic) emitters, GW bursts and stochastic sources. We present a short description of these sources below. The first class of sources, which are the subject matter of this thesis are described in more detail later in this chapter.

#### 1.3.1.1 Coalescence of compact binaries

Binaries made of neutron stars (NS) and/or black holes (BH) are the most promising sources for the GW interferometers. The different phases of the evolution of binaries may be conveniently classified as *inspiral*, *merger* and *ringdown*. Using approximation schemes in GR, one can predict very accurately the waveforms associated with the inspiral and ringdown phases. A preliminary calculation of the Newtonian waveform from inspiralling compact binaries (ICB) and the magnitude of the GW strain expected in an interferometric detector has been discussed in Sections 1 & 2.

#### 1.3.1.2 Gravitational wave bursts

These type of sources are the result of a class of unmodelled, transient and violent astrophysical phenomena like SN explosions, Gamma Ray Bursts etc. Data analysis strategies for these events involve 'excess power search' methods, where power excesses in the frequency domain are monitored or significant time variations in the amplitude of the observed signal are searched to detect the presence of burst GW. Coincidence analyses involving a network of detectors enhance the probability and reliability of the detection.

#### 1.3.1.3 Periodic gravitational wave sources

These sources are those which continuously emit GWs whose frequency remains constant over the duration of the observation. Spinning NS emitting GWs by different mechanisms are typical examples (see Ref. [17] for a review). Normal modes as a result of residual non-axisymmetric decays and accreting NS which excite non-axisymmetries (low mass x-ray binary e.g) are the two most common mechanisms which give rise to these types of sources. Data analysis for these systems involve direct searches for GW emission from known pulsars [18].

#### 1.3.1.4 Stochastic GW background

These are 'random' GW signals arising from the all-sky GW background similar to the cosmic microwave background for the electromagnetic case. This GW background radiation can be produced by different physical processes in the very early Universe (see Ref. [19] for a review . A single detector can at best put an upper limit on a stochastic background at the detector's strain noise level. To do much better, the technique is to cross correlate the outputs of detectors, taking advantage of the fact that the sources of noise in each detector will, in general, be independent. LIGO plans to use this method by comparing data sets at its two different sites. In the future, there are proposals for space-based missions entirely devoted to the stochastic background in the frequency range $0.1 - 10$ Hz. This include Big Bang Observatory (BBO) and DECIGO [20, 21].

### 1.3.2 GW Astronomy compared to EM wave astronomy

The observable properties and the production mechanisms of GW and EM waves are markedly different. This leads to very important differences in EM wave astronomy and GW astronomy. Here we list a few of them.

- EM waves interact strongly with matter. On the other hand, the gravitational interaction is the weakest of all interactions. Hence after emission of GW from a source little is absorbed on the way to the detector. This makes it possible to probe astrophysics that is electromagnetically hidden or dark. Important examples are coalescence and mergers of black-hole binaries, stellar core collapses and the dynamics of the early Universe. However, the relative strength of EM and gravitational interactions also imply that the GW are harder to detect.

- EM radiation has wavelengths which are generally smaller than the size of the source. Sources can therefore be imaged by observing the EM radiation from them. In contrast, source of GW have dimensions smaller than the wavelengths of GW emitted by them. Thus GW from sources cannot be used to create an image of the source. In this respect, GW are more similar to sound waves and the plus and cross polarisations are signatures of a stereophonic description of the dynamics of the source.

- GW have an entirely different frequency window compared to EM waves. For EM waves, the window is $10^8 - 10^{18}$ Hz ranging from the longest of the radio waves to the high energy gamma-rays. For astrophysically important GW sources, the frequency window is about $10^{-5} - 10^4$ Hz. GW at lesser frequencies are expected from early Universe processes. In the band $10^{-9} - 10^{-7}$ Hz the expected sources are the Big Bang, cosmic strings, domain walls etc. In the window $10^{-18} - 10^{-15}$ Hz, the only waves possible are relics of the Big Bang.

- Astrophysical EM signals are a signature of the thermodynamic state of the source as they are generated by incoherent superposition of waves from many emitters. On the other hand, GW signals are the result of the bulk dynamics of a dense source of mass-energy. Therefore, GW directly probe the dynamical state of the source.

- Telescopes measuring astrophysical EM signals are sensitive to the *intensity* of radiation which falls off with distance as $r^{-2}$. The directly observable quantity in the case of GW astronomy is the wave *amplitude* which falls off as $r^{-1}$. Doubling the sensitivity of a GW detector therefore doubles the distance to which sources can be detected, and increases the gravitationally accessible volume of the universe by a factor of 8.

- Solar system experiments can test GR and alternative theories of gravity in the weak field and static regime. The binary pulsar experiment, on the other hand, can probe GR in strong field and time dependent situations and distinguish between GR and tensor-multi-scalar theories of gravity [22]. GW observations also provide a unique ground for testing alternatives to GR. GW are predictions of any theory of gravity respecting special relativity. The nature of GW predicted by other metric theories of gravity are different from GR. The speed of GWs will depend on the details of the metric structure of the theory [23]. The polarisation properties of GW also depend on whether other fields are coupled to the metric. For example, Brans-Dicke theory has three states of polarisation, two transverse and one longitudinal. For a classification of the various metric theories of gravity in terms of observable properties of GW in the weak-field regime, see Ref. [24]. Therefore, detection of GW can be used to distinguish GR from alternative theories of gravity far beyond the standard solar-system tests. For example, a qualitative measurement of polarisation states of GW can rule out GR if the observations reveal more than 2 polarisation states. For a comparative study of GW and binary pulsar tests of strong gravity, see Ref. [25].

## 1.4 Data analysis of GW from Inspiralling Compact Binaries

### 1.4.1 Matched Filtering

Different noises in different frequency ranges limit the sensitivity of the interferometric types of detectors. Detector noise can conspire to appear as a signal characteristic of a binary. Alternatively it can mask the presence of a signal. The optimal design of a detector requires a detailed understanding of the different sources of noise. The dominant contributions to noise of the terrestrial detectors already in operation like LIGO, Virgo etc are from seismic, thermal and photon shot noise. At high frequencies ($> 300$ Hz) photon shot noise limits the detector sensitivity. The shot noise depends on the arm lengths, laser power and wavelength and mirror reflectivities and photo-detector efficiency in a complicated way. At intermediate frequencies ($\sim 100$Hz), the thermal noise is dominant. The source of this noise are thermal excitations of the test-mass suspensions and internal modes of the pendulum masses themselves. At low frequencies ($< 20$Hz), seismic and man-made noises are dominant. Methods such as *power recycling* and *signal recycling* are generally used in order to improve the detector performance.

Data analysis strategies for GW signals in a noisy detector vary according to the type of signal. As was mentioned in the previous Section, waveforms from ICB can be accurately predicted using approximation techniques in GR. For such signals, the data analysis technique in a noisy detector is *matched filtering* (see Ref. [26] for a review). Matched fil-

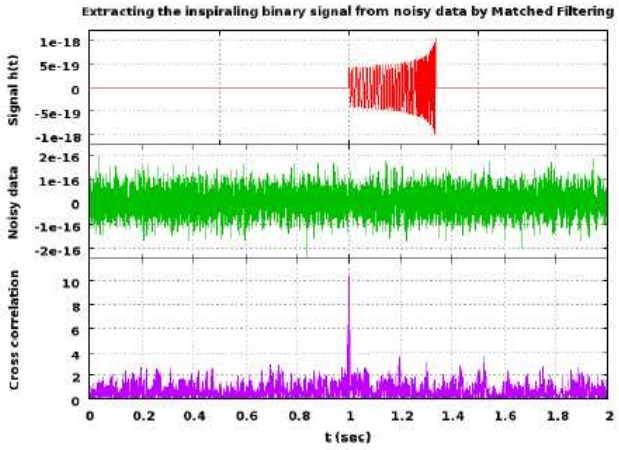


Figure 1.3: Detection by Matched Filtering of the signal from an Inspiralling Compact Binary. Precise knowledge of the GW phase evolution is needed for efficient performance of this data analysis technique. Figure courtesy: Anand Sengupta.

tering efficiently searches a weak signal of *known* form buried in noisy data. This technique consists in cross-correlating the output of a detector assumed to contain a signal of known form with a set of theoretically calculated waveforms called *templates*. The task of matched filtering involves the finding of an 'optimal' template that would produce, on average, the highest signal-to-noise ratio (SNR) (see Fig. 1.3). As seen in in Fig. 1.3, the waveform from an ICB gradually increases in amplitude and frequency with time. We will demonstrate this fact explicitly later in this Section. A signal that can be matched for a longer duration by a template helps the correlation to build up the signal power faster than noise power. Matched filtering increases the SNR in proportion to the square-root of the number of signal cycles in the detector bandwidth. A mismatch of one cycle out of $10^4$ cycles due to the use of inaccurate templates can degrade the SNR by a factor of 2. Hence, for matched filtering to be successful, it is important to have an accurate bank of templates of ICB waveforms, with particular emphasis on the accuracy of the phase evolution.

We will return to a more detailed analysis of matched filtering where we will show how to find an optimal filter for detection of a given signal and also how to extract out the parameters that characterise the signal. But before that, we will focus on the construction of templates with accurate knowledge of phasing for GW from an ICB.

### 1.4.2 Chirping of the Binary waveform & phase evolution

The phase of the Newtonian GW, from Eqs.(1.18 & 1.19) is simply $2\omega \int dt$ where $\omega$ is the orbital frequency of the binary orbit. In the first two sections we had treated $\omega$ as a *constant*. However, GW carry energy and momentum away from the source. The radiation reaction on the source leads to a gradually increasing frequency of the source. From Eqs.(1.20 & 1.21), $\omega$ also appears in the amplitude of the GW. Therefore, evolution of the binary under radiation reaction leads to a waveform whose amplitude and frequency gradually sweeps up in time. This is called a "chirp" waveform and its appearance was already depicted in Fig. 1.3.

To take into account the effect of radiation reaction, the first step is to calculate how much

energy the GW carries away from the source, *i.e.* the GW energy flux. The GW energy flux, at the leading order, is given by Einstein's quadrupole formula Eq. (1.15). The time-average over the time-scale characterising the source translates, in the case of an ICB, into an average over the orbital period. Let us first define a dimensionless variable $x$ by $x = v^2$, where $v$ is the relative velocity of the binary masses. Since we are dealing with weak GW, we expect the sources to be slowly moving. Therefore $x$ is a small quantity. For circular orbits, x can variously be written in terms of the angular velocity $\omega$ or the orbital frequency $F = \omega/2\pi$ as

$$x = v^2 = (\omega r)^2 = (m\,\omega)^{2/3} = (2\pi\, m\, F)^{2/3} \tag{1.24}$$

where we have used Kepler's law $\omega^2 r^3 = m$. In terms of $x$, the energy flux at infinity Eq. (1.15) becomes

$$L = (1/5)\langle \frac{d}{dt}\left(\ddot{I}_{i\,j}\right)\frac{d}{dt}\left(\ddot{I}_{i\,j}\right)\rangle = (32/5)\nu^2\, x^5 \tag{1.25}$$

The Newtonian conserved energy $E$ when there is no energy loss from the system is given, at the leading order, by the mechanical energy. For circular orbits it is (using Eq. (1.24))

$$E = -\frac{1}{2}\mu\, x = -\frac{1}{2}\nu\, m\, x \tag{1.26}$$

Now we invoke the energy-balance argument which is the heuristic assumption that the energy emitted from the system by GW is at the cost of an equal decrease in the energy of the system, *i.e*, $L = -\frac{dE}{dt}$.

Using the expressions for $L$ &$E$ in terms of x in the energy-balance equation, we get an expression for the rate of change of the orbital frequency which will be useful later.

$$\dot{F} = \frac{48\nu}{5\pi\, m^2}\, x^{11/2}, \tag{1.27}$$

where an over-dot indicates a time-derivative.

On integrating the energy-balance relation, but using $F$ instead of $x$, we finally obtain the evolution of the orbital frequency under radiation-reaction.

$$(2\,\pi\, F)^{-8/3} = -\frac{256}{5}\mathcal{M}^{5/3}(t - t_c) \tag{1.28}$$

$t_c$ is the time when the orbital frequency diverges, and is called the coalescence time.

From Eq. (1.28), we see that as t approaches $t_c$, $F$ also increases. Therefore the GW frequency which is $2F$ also increases with time along with the amplitude ($h \sim F^{2/3}$). This is the phenomenon of chirping and is entirely due to radiation-reaction on the binary. Notice the presence of the chirp mass $\mathcal{M}$ in Eq. (1.28). Therefore, the dynamics of the source is entirely determined, at the leading order, by the chirp-mass. We also note that the orbital frequency diverges in a finite time. This is an indication of the fact that the chirping formula should not be extended beyond a certain stage in the evolution of the binary.

Another important conclusion that can be drawn from Eq. (1.28) is the following. At a given stage of the evolution of the binary in the inspiral phase, the *larger* the chirp mass, or, roughly the total mass, the *smaller* is the orbital/GW frequency. This leads to the following classification of ICB according to the type of interferometric detectors.

- NS-NS, NS-BH, BH-BH binaries, with BH mass $\sim 10M_\odot$. These are detectable at the end of their inspiral stage, by the ground-based detectors LIGO, Virgo etc.

- Intermediate mass BH binaries $\sim (10^3 - 10^5)M_\odot$ and supermassive BH (SMBH) binaries $\sim (10^6 - 10^9)M_\odot$. These cannot be detected in their inspiral and merger stage by the ground-based detectors whose sensitivities are very poor for frequencies below 20 Hz due to seismic noise. For these sources, the proposed space-based detector LISA can be employed which will be designed to be sensitive in the bandwidth (1-$10^{-4}$) Hz.

The evolution of the orbital phase $\Phi(t) = \int \omega(t)dt = \int 2\,\pi\,F(t)dt$ under radiation reaction can be easily found from the chirping formula Eq. (1.28) as follows. We consider the quantity $\frac{d\Phi}{dF}$ which is given by

$$\frac{d\Phi}{dF} = \frac{d\Phi}{dt}/\dot{F} = \frac{5}{96}\,(2\,\pi\,\mathcal{M})^{-5/3}F^{-8/3} \tag{1.29}$$

Integrating, we obtain

$$\Phi\,[F(t)] = -\frac{1}{32}\,(2\pi\,\mathcal{M}\,F(t))^{-5/3} + \Phi_c \tag{1.30}$$

where $\Phi_c$ is another constant of integration and is the value of the orbital phase $\Phi(t)$ when the orbital frequency diverges, and is called the phase at coalescence.

### 1.4.3 Chirp Waveform in the Fourier Domain

The GW chirp signal from ICB in the time domain is now given by

$$h(t) = F_+(\theta,\phi,\psi)\,h_+(t) + F_\times(\theta,\phi,\psi)\,h_\times(t) \tag{1.31}$$

$$h_+(t) = -\frac{2\mathcal{M}^{5/3}(2\pi\,F(t))^{2/3}}{R}(1+\cos\iota^2)\cos 2\Phi(t), \tag{1.32}$$

$$h_\times(t) = -\frac{2\mathcal{M}^{5/3}(2\pi\,F(t))^{2/3}}{R}2\cos\iota\,\sin 2\Phi(t). \tag{1.33}$$

where the time-evolution of the orbital frequency and orbital phase are given by Eqs. (1.28) &(1.30) respectively. We will now calculate the Fourier transform (FT) of this waveform. Our motivation is to re-address the issue of matched filtering in the Fourier domain. A Fourier domain analysis is preferred because of two reasons. Firstly, since the exact arrival time of the signal is not known, an arbitrary time shift parameter will be present in the time-domain waveform. This parameter appears naturally as a shift in phase in the Fourier domain and is easy to deal with. Secondly, correlation in the time domain is an optimum statistic only if the noise is *white* (independent of frequency), which is never the case. If the noise is stationary, which we will assume, the noise at different frequencies will be uncorrelated.

Before we proceed in our calculation of the FT of Eq.(1.31), we need to revisit Eq. (1.27). From the expression of $\dot{F}(t)$, one can construct a radiation-reaction time scale $\tau_{RR}$ given by $\tau_{RR} = F/\dot{F}$. Then the ratio of the orbital period $P$ to $\tau_{RR}$ becomes

$$\frac{P}{\tau_{RR}} = 1/(F\,\tau_{RR}) = \frac{\dot{F}}{F^2} \sim x^{5/2} \tag{1.34}$$

which is a small quantity for weakly stressed sources. Therefore, the orbital time scale is small compared to the radiation-reaction time scale. This allows us to use the Stationary Phase Approximation (SPA) to obtain an analytic expression for the FT of Eq.(1.31). To this end, we first write $h(t)$ as a pure cosine term

$$h(t) = -\frac{2\mathcal{M}^{5/3}(2\pi F(t))^{2/3}}{R} A_{(2,0)} \cos[2\Phi(t) + \phi_{(2,0)}] \tag{1.35}$$

where $A_{(2,0)}$ and $\phi_{(2,0)}$ functions of $(\nu, \theta, \phi, \psi, \iota)$. Now, ground-based detectors can detect GW from NS-NS and NS-BH binaries only at the late stage of their inspiral phase. The GW signal lasts for a few minutes in the detector bandwidth. For such short-lived signals we can neglect Earth's orbital motion during the time of observation. This essentially means that in a coordinate system fixed to the detector, the source angular coordinates can be treated as constants. The FT of the GW $\tilde{h}(f)$ is given by

$$\tilde{h}(f) = \int_{-\infty}^{\infty} h(t) e^{2\pi \mathbf{i} f t} dt \sim -\int_{-\infty}^{\infty} \frac{\mathcal{M}^{5/3}(F(t))^{2/3}}{R} \left( e^{2\pi \mathbf{i}(f t + 2\Phi(t))} + e^{2\pi \mathbf{i}(f t - 2\Phi(t))} \right) dt \tag{1.36}$$

Now the amplitude of the Fourier integrals in Eq. (1.36) (containing the orbital frequency $F(t)$) varies on radiation reaction time-scales while the phase varies on orbital time-scales. We can therefore use the SPA to evaluate the two terms in the above Fourier integral. Since $\Phi(t)$ increases monotonically with time, there is no stationary point of the phase in the first term. Therefore, to the leading order in the asymptotic expansion, this term does not contribute to $\tilde{h}(f)$. For the second term, the stationary point of the phase, for a given value of the transform variable $f$ is at the time defined implicitly by

$$F(t) = f/2. \tag{1.37}$$

Therefore, the contribution to $\tilde{h}(f)$ at a given value of $f$ comes from the neighbourhood of time when the orbital frequency $F(t)$ sweeps past the value $f/2$. The final result of the SPA Fourier domain waveform $\tilde{h}(f)$ is given by

$$\tilde{h}(f) \simeq -\frac{\mathcal{M}^{5/3}(F(t(f/2)))^{2/3}}{R\sqrt{2\dot{F}(t(f/2))}} A_{(2,0)} \exp\left[ i\, \psi_f(t(f/2)) \right] e^{-i\phi_{(2,0)}}, \tag{1.38}$$

where $\psi_f(t(f/2))$ is given by

$$\psi_f(t(f/2)) = 2\pi f\, t(f/2) - 2\,\Phi(t(f/2)) - \pi/4 \tag{1.39}$$

The notation $t(f/2)$ means the time when the orbital frequency reaches the value $f/2$. Using Eqs. (1.28) &(1.30), the phase $\psi_f(t(f/2))$ of the Fourier domain waveform $\tilde{h}(f)$ reduces to

$$\psi_f(t(f/2)) = \frac{3}{128} (\pi\, \mathcal{M}\, f)^{-5/3} + 2\pi f\, t_c - 2\,\Phi_c - \pi/4 \tag{1.40}$$

Radiation reaction, resulting in increase of $F(t)$ drives the binary system beyond the inspiral phase where the above waveform is incorrect. We truncate $h(t)$ beyond $t_{\rm LSO}$, which is the time when $F(t)$ reaches $F_{\rm LSO}$ – the orbital frequency at the LSO in test-particle limit.

$F_{\rm LSO}$ is given by

$$F_{\rm LSO} = (2\,\pi\,6^{\frac{3}{2}}\,m)^{-1} \tag{1.41}$$

### 1.4.4 Matched Filtering: Fourier Domain

Having obtained the FT of the GW we return to matched filtering of GW from ICB, but in the frequency domain (for an analysis more detailed than presented here, see Ref. [27]). The output of a noisy gravitational wave detector is

$$x(t) = h(t) + n(t)\,, \tag{1.42}$$

where $h(t)$ is the deterministic GW signal given at the leading order by Eq. (1.31) and $n(t)$ is the noise, which we assume to be a stationary Gaussian random variable, with zero mean. Let $q(t)$ be a linear filter/template and $c(t)$ be its correlation with the total detector output $x(t)$

$$c(t) = \int_{-\infty}^{\infty} dt'\; x(t')\,q(t+t')\,. \tag{1.43}$$

Let us define another new quantity $\sigma[q](t)$ such that the correlation $c(t)$ is normalized by the square root of its variance,

$$\sigma[q](t) = \frac{c(t)}{\left[\overline{c^2(t)} - \overline{c(t)}^2\right]^{1/2}} = \frac{2\Re\int_0^\infty df\;\tilde{x}(f)\,\tilde{q}^*(f)\,e^{2\pi i f t}}{\left[\int_0^\infty df\,S_h(f)\,|\tilde{q}(f)|^2\right]^{1/2}}, \tag{1.44}$$

where $\tilde{x}(f)$ and $\tilde{q}(f)$ are the Fourier transforms of $x(t)$ and $q(t)$, respectively. An overbar denotes the ensemble average over many realisations of the noise. The quantity $S_h(f)$ is the real, *one-sided* power spectral density of the detector defined only for positive frequencies by

$$\overline{n(f)\tilde{n}^*(f')} = \frac{1}{2}\delta(f-f')\,S_h(f)\,, \tag{1.45}$$

and $\tilde{n}(f)$ is the Fourier transform of the noise $n(t)$ . The filtered SNR $\rho$ is defined by the ensemble average

$$\rho[q](t) = \overline{\sigma[q](t)} = \frac{2\Re\int_0^\infty df\;\tilde{h}(f)\,\tilde{q}^*(f)\,e^{2\pi i f t}}{\left[\int_0^\infty df\,S_h(f)|\tilde{q}(f)|^2\right]^{1/2}}. \tag{1.46}$$

An optimal filter/template is defined as the one which maximises the SNR at a particular instant, say $t = 0$, and is given by the matched filtering theorem as

$$\tilde{q}(f) = \gamma\,\frac{\tilde{h}(f)}{S_h(f)}\,, \tag{1.47}$$

where $\gamma$ is an arbitrary real constant. The SNR corresponding to the optimal filter is therefore

$$\rho^2 = 4\int_0^\infty df\,\frac{|\tilde{h}(f)|^2}{S_h(f)}. \tag{1.48}$$

### 1.4.5 Parameter Estimation

The GW signal from ICB depends on the parameters of the source. The waveform at the leading order given by Eqs. (1.31) in the time-domain or by Eqs. (1.38) in the Fourier domain depend on the parameters of the source like the chirp mass, the angular coordinates of the source, distance to the detector etc. The problem of detection consisted of finding out whether a signal of known form but undetermined parameters was present in the noisy detector output or not. The problem of parameter estimation *assumes* the presence of a signal in the detector and attempts to characterise it in terms of the source parameters.

To this end, we maximise the correlation in Eq. (1.44) with an entire family of templates which correspond to different possible values of the source parameters. The template parameters which maximise the correlation are defined as the *measured* values characterising the signal. These parameters will not necessarily be equal to the *true* parameters of the signal present in the detector. This is because for a given signal, different realizations of the noise will give rise to different best-fit parameters. However, for large SNR, the best-fit parameters follow a Gaussian distribution with mean values equal to the actual values.

Let $\tilde{\theta}^a$ denote the 'true values' and $\tilde{\theta}^a + \Delta\theta^a$ be the best-fit values of the parameters respectively. Then for large SNR, errors in the estimation of parameters $\Delta\theta^a$ obey a Gaussian probability distribution of the form [28]

$$p(\Delta\theta^1, \cdots \Delta\theta^n) = p^{(0)} e^{-\frac{1}{2}\Gamma_{bc}\Delta\theta^b\Delta\theta^c}, \tag{1.49}$$

where $p^{(0)}$ is a normalization constant and $n$ the number of parameters. In the above expression $\Gamma_{ab} \equiv (h_a \,|\, h_b)$ is the *Fisher information matrix* evaluated at the *measured* value of the parameters, $h_a$ being $\partial h/\partial\theta^a$,. The symbol $(\,|\,)$ denotes the noise weighted inner product defined for any two functions $g$ and $h$ as:

$$(g \,|\, h) \equiv 2 \int_0^\infty df\, \frac{\tilde{g}^*(f)\,\tilde{h}(f) + \tilde{g}(f)\,\tilde{h}^*(f)}{S_h(f)}. \tag{1.50}$$

Using the above definition of the inner product we re-express $\Gamma_{ab}$ as

$$\Gamma_{ab} = 2 \int_0^\infty \frac{\tilde{h}_a^*(f)\tilde{h}_b(f) + \tilde{h}_a(f)\tilde{h}_b^*(f)}{S_h(f)}\, df. \tag{1.51}$$

The variance-covariance matrix, or simply the covariance matrix, is defined as the inverse of the Fisher information matrix. It is given by

$$\Sigma^{ab} \equiv \langle \Delta\theta^a \Delta\theta^b \rangle = (\Gamma^{-1})^{ab}, \tag{1.52}$$

where $\langle\cdot\rangle$ denotes an average over the probability distribution function in Eq. (1.49). The root-mean-square error $\sigma_a$ in the estimation of the parameter $\theta^a$ is

$$\sigma_a = \left\langle (\Delta\theta^a)^2 \right\rangle^{1/2} = \sqrt{\Sigma^{aa}}\,. \tag{1.53}$$

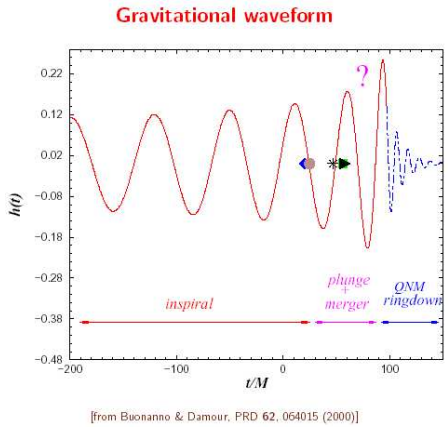


Figure 1.4: The three stages in the evolution of compact binaries. The inspiral stage is accurately modelled by postNewtonian theory. The merger stage has recently been computed using Numerical Relativity. The final ringdown stage waveform can be calculated using BH perturbation techniques. Adapted from Ref. [29]

The correlation coefficient $c^{ab}$ between two parameters $\theta^a$ and $\theta^b$ is defined as

$$c^{ab} = \frac{\langle \Delta\theta^a \Delta\theta^b \rangle}{\sigma_a \sigma_b} = \frac{\Sigma^{ab}}{\sqrt{\Sigma^{aa}\Sigma^{bb}}}. \tag{1.54}$$

(There is no summation over repeated indices in Eqs. (1.53) and (1.54).) By their definition, the correlation coefficients lie in the range $[-1, 1]$. When the correlation coefficient between two parameters is close to 1 (or $-1$), it indicates perfect correlation (or anti-correlation) between the two parameters. A value close to 0 indicates that the two parameters are uncorrelated.

## 1.5 Accurate templates for different phases of binary evolution: inspiral, merger and ringdown

In this Section we focus on the three phases of the binary dynamics, *i.e*, inspiral, merger and ringdown. We discuss each of these stages with particular emphasis on the theoretical tools necessary for calculation of templates for data-analysis of GW. See Fig. 1.4 for a schematic representation of the GW from each of the three phases.

### 1.5.1 Inspiral

This is the preliminary stage of the binary evolution where it loses energy and angular momentum via emission of GW and spirals in. The *adiabatic* approximation, where the gravitational radiation reaction time scale is longer than the orbital time scale, is a valid approximation during this phase. This phase continues approximately all the way up to an orbital separation of $r \simeq 6\,m$, the LSO in the test-particle limit. The gravitational waveform from this adiabatic inspiral is well modelled within GR using Multipolar Post Minkowskian

(MPM) approximation and matching to a post-Newtonian (PN) source (see [30] for a review), where the relevant physical quantities are expressed as a perturbative series in powers of $v/c$, $v$ being the relative velocity assumed to be small. A detailed description of the PN approximation scheme is provided in Sections 2.1 and 2.2 of Chapter 4.

The MPM approximation scheme takes into account nonlinearities of the Einstein's equations upto a finite order. After matching to a PN source, it introduces corrections to the leading order (called Newtonian) expressions of the time domain waveform Eq. (1.31) and also corrections to the Quadrupole formula Eqs. (1.15), (1.25) & (1.26). The general formalism applies to regular sources but application to ICB is efficiently implemented by modelling the source as two structureless point particles. This entails an independent and new technical complication related to the regularisation of self-field effects in the computation. Some relevant details of this are summarised in Chapter 4. This treatment implies neglect of the effects of finite size and quadrupole distortion induced by tidal interactions. A calculation of the effect of the Newtonian quadrupole moments (induced by mutual tidal interactions) of the binary components leads to a correction in the GW phase which is at 5PN order beyond the leading Newtonian term in Eq. (1.30) of chapter 1. The finite-size GW phase is [30]

$$\Phi\left[F(t)\right]_{\text{finite size}} = -\frac{1}{32}\left(2\pi\,\mathcal{M}\,F(t)\right)^{-5/3}\left[1+\cdots+\text{const.}\,k\left(\frac{x}{K}\right)^{5}\right]+\Phi_c \tag{1.55}$$

where $k$ is the Love number and $K$ the compactness of the binary components, assumed to have equal masses. Even though the finite-size term in Eq. (1.55) is a Newtonian effect (independent of $c$), for a NS-NS binary ($K\sim 0.2$ and $k'=\text{const.}\,k\sim 1$) this term is numerically comparable to a 5PN correction to the leading order radiation-damping term. Since the GW phase is currently known upto 3.5PN order only (see below), the point-particle assumption of PN theory is sufficient when applied to NS and/or BH binaries (the argument however breaks down for even moderately compact objects like white dwarfs for which the finite-size term dominates over the leading term in Eq. (1.55)). See also Ref. [31] for a general-relativistic treatment of the "effacing" of the strong self-field of the compact objects when regarding their orbital motion.

At present the energy flux is known upto 3.5PN order and the conserved energy upto 3PN order[1]. Using the energy balance equation as in Section 4.2, one arrives at 3.5PN accurate expressions for the chirping formula Eq. (1.28) and orbital phase Eq. (1.30) [32]. For the phase of the Fourier domain waveform $\tilde{h}(f)$ (Eq. (1.38)) given at the Newtonian order by Eq. (1.56), the 3.5PN accurate expression is

$$\psi_f(t(f/2)) = 2\pi f\,t_c - 2\,\Phi_c - \pi/4 + \frac{3}{128}\left(\pi\,\mathcal{M}\,f\right)^{-5/3}\sum_{k=0}^{7}\alpha_k\,x_f^{k/2} \tag{1.56}$$

where $x_f = x(t(f/2)) = (\pi\,m\,f)^{2/3}$. The coefficients $\alpha_k$'s, $k=0,\ldots,7$, (with $x^{7/2}$ signifying 3.5PN order) are given by

$$\begin{aligned}\alpha_0 &= 1,\\ \alpha_1 &= 0,\end{aligned}$$

[1] As usual, we refer to $n$PN as the order equivalent to terms $\sim (v/c)^{2n}$ in the asymptotic waveform (beyond the Einstein quadrupole formula), where $v$ denotes the binary's orbital velocity and $c$ is the speed of light.

$$
\begin{aligned}
\alpha_2 &= \frac{20}{9}\left(\frac{743}{336}+\frac{11}{4}\nu\right),\\
\alpha_3 &= -16\pi,\\
\alpha_4 &= 10\left(\frac{3058673}{1016064}+\frac{5429}{1008}\,\nu+\frac{617}{144}\,\nu^2\right),\\
\alpha_5 &= \pi\left(\frac{38645}{756}+\frac{38645}{252}\,\log\left(\frac{v}{v_{\rm lso}}\right)-\frac{65}{9}\nu\left[1+3\log\left(\frac{v}{v_{\rm lso}}\right)\right]\right),\\
\alpha_6 &= \left(\frac{11583231236531}{4694215680}-\frac{640\,\pi^2}{3}-\frac{6848\,C}{21}\right)+\nu\left(-\frac{15335597827}{3048192}+\frac{2255\,\pi^2}{12}\right.\\
&- \left.\frac{1760\,\theta}{3}+\frac{12320\,\lambda}{9}\right)+\frac{76055}{1728}\nu^2-\frac{127825}{1296}\nu^3-\frac{6848}{21}\log(4\,v),\\
\alpha_7 &= \pi\left(\frac{77096675}{254016}+\frac{378515}{1512}\,\nu-\frac{74045}{756}\,\nu^2\right),
\end{aligned}
\tag{1.57}
$$

where $C(=0.577216\cdots)$ is Euler's constant, $v=\sqrt{x}$, $v_{\rm lso}=\frac{1}{\sqrt{6}}$, $\theta=-\frac{11831}{9240}$ & $\lambda=-\frac{1987}{3080}$.

The MPM formalism supplemented by matching to a PN source, modelling ICB by point particles and a suitable self-field regularisation provides corrections to the amplitude of the GW in Eq. (1.31), apart from the 3.5PN accurate GW phase in Eq. (1.56). These are called amplitude-corrections and the frequency corresponding to these corrections are not necessarily twice the orbital frequency of the binary. For purposes of matched filtering (which is sensitive to the wave phasing), it has been common practice to keep only the Newtonian amplitude in Eq. (1.31) and the phase $\Phi(t)$ in Eq. (1.31) (or the phase $\psi_f(t(f/2))$ in Eq. (1.38)) upto 3.5PN order given by Eqs. (1.56) & (3.4.3). This waveform is called the *Restricted Wave Form* (RWF). In Chapters 2 & 3 we go beyond the RWF, where we consider the data-analysis of SMBH binaries with amplitude-corrected waveforms.

The late inspiral (where the relative velocity of the binary becomes relativistic $\sim 0.3$) and plunge is a regime where the convergence of the PN series progressively degrades and eventually the PN approximation scheme breaks down. Resummation methods like Padé approximants have been suggested as a tool to improve the convergence properties of the PN series [33, 34, 35]. The effective one body method proposed by Buonanno and Damour [36, 29] provides an analytical method to study the transition from the inspiral to plunge.

### 1.5.2 Merger

The adiabatic inspiral is followed by the late inspiral and merger of the two bodies. To model this phase and construct reliable templates for it requires a numerical solution of the *full* Einstein equations. Recent advances in Numerical Relativity (NR) [37, 38, 39, 40] has resulted in breakthroughs in the computation of the late inspiral and subsequent merger and ringdown phases. Ref. [37] treats a binary BH evolution using on a numerical code based on generalized harmonic coordinates. The angular momentum parameter of the resultant BH after coalescence was estimated to be $a\approx 0.70$. It also concluded that about 5% of the initial rest mass will be radiated during the final orbit and ringdown.

A new field has emerged recently consisting of high-accuracy comparisons between the PN predictions and the NR waveforms. Such comparisons have proved currently to be very successful [41, 42, 43, 44, 45]. Ref. [45] studied the evolution in the last few orbits and

merger of a binary BH system for a wide variety of initial separations. The result of their simulations was the formation of a final BH with spin parameter 0.69. By plotting the frequencies as function of time, they found excellent agreement between their simulations and 2PN results.

### 1.5.3 Ringdown

The final stage in the evolution of compact binaries is the ringdown phase. In this stage, the two merged objects form a resultant BH (or a NS) and settles down to a quiescent state by radiating the assymetries in the form of GWs. These gravitational waveforms are computed using BH perturbation methods. If the resultant of the merger is a BH, then the ringdown waveform is completely determined by its mass and spin only. If the final object is a NS, the waveform depends on the equation of state of the NS material. See Ref. [46] for a review.

## 1.6 Inspiralling compact binaries on eccentric orbits

In this section we give a brief introduction to ICB whose orbits are noncircular, *i.e.*, eccentric. All our previous analyses were restricted to ICB moving in circular orbit. These are the most plausible sources of GW for laser interferometric GW detectors for the following reason. ICB moving in elliptical orbits with large relative separation circularise under radiation reaction due to loss of energy through emission of GW, a result obtained by Peters [47]. When GW from these binaries reach the detector bandwidth they have already lost all their eccentricity. However astrophysical investigations indicate the possibility of detecting binaries with eccentricity in the sensitive bandwidth of both terrestrial and space-based gravitational wave detectors. One of the most important mechanisms which could make the eccentricity of the binary non-zero, even towards late stages of their inspiral, is the Kozai mechanism [48]. This occurs in cores of dense globular clusters where gravitational interactions between *pairs* of binary BH systems are likely. These interactions can lead to the formation of a stable three-body configuration, where two closely bound BH orbit each other while the third orbits the center-of-mass of the first two. Tidal forces from the outer BH increases the eccentricity of the inner stable binary by causing an orbital resonance. The Kozai mechanism can lead to eccentricities greater than 0.1 at the time GW from the inner binary enters the bandwidth of Advanced LIGO [49]. A more detailed survey of the possible mechanisms which will produce binaries with non-negligible eccentricity and an update of the data analysis strategies in dealing with the GW signals from these sources have been provided in Section 1 of Chapter 5. The theoretical inputs needed to construct the templates for eccentric binaries have also been discussed in detail in Chapter 5.

To see the effect of eccentricity on our previous analysis, we start with a concrete example, the famous Hulse-Taylor binary pulsar PSR 1913+16. It comprises a 59 ms pulsar and an unseen companion star. Time-of-arrival measurements of pulses from PSR 1913+16 lead to an accurate velocity curve from which Hulse & Taylor concluded that the binary orbit has a period $P_b = 7.75\,\mathrm{hr} \pm 7\mathrm{s}$ and a high eccentricity $e = 0.615 \pm 0.010$ [3]. Observations of the pulse arrival times from 1974 to 1981 show a secular decay in the orbital period, the decay rate being measured to be $\dot{P}_b(\mathrm{observed}) = (-2.30 \pm 0.22) \times 10^{-12}$ [50]. Radiation reaction leads to a secular increase in the orbital frequency of the binary orbit and a corresponding

secular decrease in the period. If we neglect the eccentricity of the system, the theoretical prediction for orbital period change due to emission of quadrupole gravitational radiation from a binary in a circular orbit is given by, from Eq. (1.27)

$$\dot{P}_b = -\frac{192\,\pi\,G^{5/3}}{5\,c^5}\left(\frac{2\pi}{P_b}\right)^{5/3}\mathcal{M}^{5/3} = -\frac{192\,\pi\,G^{5/3}}{5\,c^5}\left(\frac{2\pi}{P_b}\right)^{5/3}\frac{m_p\,m_c}{(m_p+m_c)^{1/3}} \tag{1.58}$$

where we have inserted the G's and c's for convenience. In Eq. (1.58), $m_p = 1.42 \pm 0.06 M_\odot$ and $m_c = 1.41 \pm 0.06 M_\odot$ are the masses of the pulsar and the companion star respectively which have been calculated from the measurements of the observed orbital elements of the binary in Ref. [50]. Inserting the values of $P_b\,, m_p\,\&\,m_c$ in Eq. (1.58) we get the theoretical prediction of the orbital period derivative for circular orbits to be $\dot{P}_b = (-2.029 \pm 0.005) \times 10^{-13}$, which is an order of magnitude smaller than $\dot{P}_b$(observed). Therefore, a binary in an eccentric orbit loses *more* energy through GW emmision than a binary with same individual masses and orbital period, but whose orbit is circular.

Let us now take into account the eccentricity of the orbit. Starting from Eq. (1.10) but using the relative separation vector as $\mathbf{x} \equiv (x, y, z) = (r\cos V, r\sin V, 0)$, where $V$ is the true anomaly (the polar angle in plane-polar coordinates in the orbital plane). The orbital separation $r$ is related to the true anomaly $V$ by

$$r = \frac{a(1-e^2)}{1+e\cos V},$$

where $a$ is the major-axis and $e$ is the eccentricity of the elliptical binary orbit. Using these in Eq. (1.10) we obtain the generalisations of the Newtonian waveform (Eqs. 1.20 & 1.21) for elliptical orbits. Calculating the energy flux averaged over a period and using the energy-balance equation we finally get the GR prediction for the secular orbital period derivative $\dot{P}_b$(theory) as

$$\dot{P}_b(\text{theory}) = -\frac{192\,\pi\,G^{5/3}}{5\,c^5}\left(\frac{2\pi}{P_b}\right)^{5/3}\frac{m_p\,m_c}{(m_p+m_c)^{1/3}}\frac{1}{(1-e^2)^{7/2}}\left(1+\frac{73}{24}e^2+\frac{37}{96}e^4\right) \tag{1.59}$$

We now insert the values of $P_b\,, m_p\,\&\,m_c$ in Eq. (1.59) to obtain the theoretical prediction $\dot{P}_b(\text{theory}) = (-2.403 \pm 0.005) \times 10^{-12}$, which is in excellent agreement with the observed value $\dot{P}_b(\text{observed}) = (-2.30 \pm 0.22) \times 10^{-12}$.

## 1.7 LISA

In Section 1.4.1, we had mentioned that seismic noise limits the sensitivity of ground based detectors below 20Hz. To detect low frequency GW ($\leq$ 1Hz) a space based GW interferometric detector called Laser Interferometer Space Antenna (LISA) is planned [51]. It will be designed to be sensitive to GWs of frequency $10^{-5} - 1$Hz [52, 53]. Typical sources in this frequency band include a wide variety of short period binaries (both galactic and extra galactic), stochastic GW, extreme mass ratio inspirals of a stellar mass BH falling into a supermassive BH (SMBH) companion and inspiral and consequent merger of two SMBH binaries.

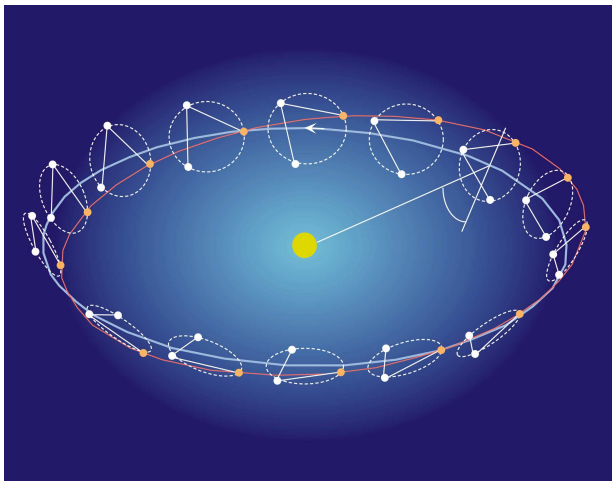

Figure 1.5: The LISA orbit is heliocentric with a 60° inclination with the ecliptic (the blue circle). The three sattelites containing the test-masses maintain an equilateral triangle configuration. Figure downloaded from the LISA website– http://lisa.jpl.nasa.gov.

### 1.7.1 LISA's configuration and properties

LISA is a (equilateral) triangular space craft configuration, whose distance between adjacent arms is 5 million kilometers. LISA will orbit around the Sun with a 20° lag w.r.t the Earth. It will have a tilt of 60° with the ecliptic plane. See Fig. 1.5 for an illustration. Each space craft carries suspended test-masses and mirrors. Like the ground based detectors, LISA is not a 'pointed instrument' but an all-sky monitor with a quadrupolar antenna pattern. Ground based detectors have two arms, the time-varying arm-length difference due to an incident GW is measured interferometrically. The measurable quantity for them is a linear combination of the two polarizations. On the other hand, LISA, with its three arms, can construct two such linearly independent arm-length differences and will be able to measure *both* the polarizations of the incident GW *simultaneously*.

For triangulating a source in the sky with the ground based detectors, one requires a three detector network. The orbital motion of LISA induces frequency, phase and amplitude modulations in the observed GW signal. These modulations carry information about both the source's location and orientation. The amplitude modulation is caused by the change in the detector's beam pattern functions in the sky due to the orbital motion. Translational motion of the detector w.r.t the source during its orbital motion around the Earth causes Doppler effect induced frequency modulations. (See [54] for a discussion about these effects and extraction of information from them during data-analysis). We provide the amplitude and phase modulated GW signal in Chapter 2.

Maintaining the giant LISA configuration in space is a challenging task. It is impossible to bounce the laser beams between different arms because of the extremely large arm lengths (compared to LIGO-Virgo etc.) involved. Hence Doppler tracking will be employed to track the space crafts with laser beams. Phase fluctuations in the master laser causes laser phase noise which is the most important noise source for LISA. Since it is impossible to maintain equal arm lengths, the cancellation of laser phase noise is a non-trivial issue. To overcome this problem, one has to combine different data streams with appropriate time delays so as to cancel the laser noise. This is called time delay interferometry (TDI) [55, 56, 57] (See [58]

for a review). By properly time shifting the data generated by each readout, one can construct observable which are not insensitive to the laser phase noise and optical bench motions. In Chapters 2 & 3, where we investigate data-analysis aspects of SMBH binaries with LISA, we shall bypass the use of TDI variables by working with a simplified assumption that noises in the two independent LISA detectors are uncorrelated.

### 1.7.2 Supermassive black-hole binaries & LISA

There is strong observational evidence for the existence of SMBH with masses in the range of $10^6 M_\odot$–$10^9 M_\odot$ (see e.g. Ref. [59] and references therein) in most galactic nuclei [60]. Therefore, mergers of galaxies, as evidenced by high-redshift surveys, should give rise to binaries containing SMBH. Evolution of a SMBH binary is governed by the emission of GW. The resulting loss of orbital energy and angular momentum from the binary results in the merger and coalescence of the two holes. GW emitted by SMBH binaries at high redshifts fall in the LISA bandwidth and their observation is one of the major science goals of LISA. These observations will allow us to probe the evolution of SMBH and structure formation [61] and provide an unique opportunity to test General Relativity (and its alternatives) in the strong field regime of the theory [62, 63, 64, 65, 66]. Observing SMBH coalescences with high (100-1000) SNR [64, 65] 'is crucial for performing all the aforementioned tests.

Since LISA can determine the location and orientation of the source from the information encoded in the amplitude and phase modulations, it can determine the luminosity distance of SMBH binaries. Therefore, SMBH binaries are often referred to as GW "standard sirens" (analogous to the electromagnetic "standard candles") [67]. LISA would also be able to measure the "redshifted" masses of the component BH apart from the luminosity distance with good accuracy for sources up to redshifts of a few. However, GW observations alone cannot provide any information about the redshift of the source. If the host galaxy or galaxy cluster is known one can disentangle the redshift from the masses by optical measurement of the redshift. This would not only allow one to extract the "physical" masses, but also provide an exciting possibility to study the luminosity distance-redshift relation providing a totally independent confirmation of the cosmological parameters. Further, this combined observation can be used to map the distribution of BH masses as a function of redshift [61, 62, 63].

Another outstanding issue in present day cosmology in which LISA can play a role is the dark energy and its physical origin (see, e.g., Ref. [68] for a review). Probing the equation-of-state-ratio ($w$(z)) provides an important clue to the question of whether dark energy is truly a cosmological constant (i.e., $w = -1$). Assuming the Universe to be spatially flat, a combination of WMAP and Supernova Legacy Survey (SNLS) data yields significant constraints on $w = -0.967^{+0.073}_{-0.072}$ [1]. Without including spatial flatness as a prior, WMAP, large-scale structure and supernova data place a stringent constraint on the dark energy equation-of-state, $w = -1.08 \pm 0.12$. LISA could play an important role in investigating the nature of dark energy as argued in Refs. [69, 70]. LISA's observation of certain binary SMBH coalescence events could constrain the dark energy equation of state to within a few percent, comparable to the level expected from other dark energy missions as quoted above. Chapter 3 revisits this problem and shows that the science potential is enhanced if one uses templates which includes amplitude corrections beyond the RWF.